Engineering bioprintable alginate/gelatin composite hydrogels with tunable mechanical and cell adhesive properties to modulate tumor spheroid growth kinetics

Engineering bioprintable alginate/gelatin composite hydrogels with tunable mechanical and cell adhesive properties to modulate tumor spheroid growth kinetics

Tao Jiang[1,7,‡], Jose G. Munguia-Lopez[2,5,‡], Kevin Gu[3], Maeva M. Bavoux[6], Salvador Flores-Torres[2], Jacqueline Kort-Mascort[2], Joel Grant[4], Sanahan Vijayakumar[4], Antonio De Leon-Rodriguez[5], Allen J. Ehrlicher[2], Joseph M. Kinsella[2,]*

[1] Department of Mechanical Engineering, [2] Department of Bioengineering, [3] Department of Chemical Engineering, and [4] Department of Materials Engineering, McGill University, 817 Sherbrook Street West, Montreal, Quebec, H3A 0C3, Canada

[5] Department of Molecular Biology, Instituto Potosino de Investigación Científica y Tecnológica, A.C. (IPICyT), Camino a la Presa San José 2055, Lomas 4 Sección, San Luis Potosi, San Luis Potosi, 78216, Mexico

[6] Department of Bioengineering, Institution of Ecole Polytechnique Fédérale de Lausanne (EPFL), Route Cantonale, Lausanne, 1015, France

[7] Department of Mechanical Engineering, National University of Defense Technology, Changsa, China

‡These authors contributed equally to this work

KEYWORDS: Tumor spheroids, bioprinting, composite hydrogel, alginate, gelatin

ABSTRACT: Tunable bioprinting materials are capable of creating a broad spectrum of physiological mimicking 3D models enabling *in vitro* studies that more accurately resemble *in vivo* conditions. Tailoring the material properties of the bioink such that it achieves both bioprintability and biomimicry remains a key challenge. Here we report the development of engineered composite hydrogels consisting of gelatin and alginate components. The composite gels are demonstrated as a cell-laden bioink to build 3D bioprinted *in vitro* breast tumor models. The initial mechanical characteristics of each composite hydrogel are correlated to cell proliferation rates and cell spheroid morphology spanning month long culture conditions. MDA-MB-231 breast cancer cells show gel formulation-dependency on the rates and frequency of self-assembly into multicellular tumor spheroids (MCTSs). Hydrogel compositions comprised of decreasing alginate concentrations, and increasing gelatin concentrations, result in gels that are mechanically soft and contain a greater number of cell-adhesion moieties driving the development of large MCTS; conversely gels containing increasing alginate, and decreasing gelatin concentrations are mechanically stiffer, with fewer cell-adhesion moieties present in the composite gels yielding smaller and less viable MCTS. These composite hydrogels can be used in the biofabrication of tunable *in vitro* systems that mimic both the mechanical and biochemical properties of the native tumor stroma.

1. INTRODUCTION

Hydrogels, hydrophilic polymeric materials capable of holding a large amount of water in their 3D network, have been widely used in bioprinting due to their favorable printability, biomimicry,

and biocompatibility[1, 2]. Many hydrogel systems have been developed to create three dimensional cell microenvironment, such as alginate, gelatin, chitosan, hyaluronic acid, PEG derivatives, etc[3-6]. Alginate and gelatin are among the most commonly used hydrogel bioinks for extrusion-based printing to recreate solid tissue-like physiological models[7-11]. Gelatin denatured from collagen provides bioactive amino acid residues enabling cell adherence. It also features a reversible thermal-dynamic trait that allows it to form triple-helix structure when the temperature is lowered[12], which results in solidification of gelatin solution with significantly increased modulus and viscosity[13]. On the other hand, alginate is a bioinert polysaccharide that can be ionically crosslinked by divalent cations to provide matrix integrity at physiological temperature[14]. The concentration of alginate solutions can result in significantly different flowabilities as well as post-crosslinking matrix elasticity. Wei Sun's group has studied the printability of different concentrations of alginate and gelatin as well as cell survival/viability following shear stress during extrusion bioprinting[11, 15]. It is noteworthy that the cells have the potential to recover from short-term membrane damage and continue to proliferate during extended periods of culture, where matrix elasticity and adherence potential can play prominent roles[16, 17]. The composite hydrogels comprised of alginate and gelatin have the potential to tune these post-printing mechanical and biological properties by varying the initial concentrations of the two components. The tunability of these hydrogels can eventually result in applications in various fields such as building disease models, tissue regeneration, and drug testing.

One of these applications is recreating the tumor microenvironment (TME). The TME is a highly dynamic system, and cells respond to the homeostasis by regulating the extracellular matrix (ECM) properties such as local elasticity and cell-matrix adhesion potential[18-22]. During the onset of malignancy, cancer cells often aggregate and assemble into multicellular tumor spheroids

(MCTS)[23-25]. Recreating the TME, and facilitating the formation of MCTS *in vitro*, is challenging using conventional two-dimension (2D) cell culture techniques. Comparisons of 2D and 3D cultures of cancer cells demonstrate that the cells retain physiologically relevant morphologies, and aggregate into MCTS, which could result in increased drug resistance in 3D cultures[26-36]. Numerous methods including hanging drop, non-adhesive surface coating, rotary bioreactors, mold casting, and 3D bioprinting have recently been developed to engineer the 3D *in vitro* environment to promote MCTS generation[26, 27, 29, 37-45]. Amongst these approaches, 3D bioprinting is advantageous as it features controllable reference locations for cells, the ability to use high cell densities, and reproducibility among samples.

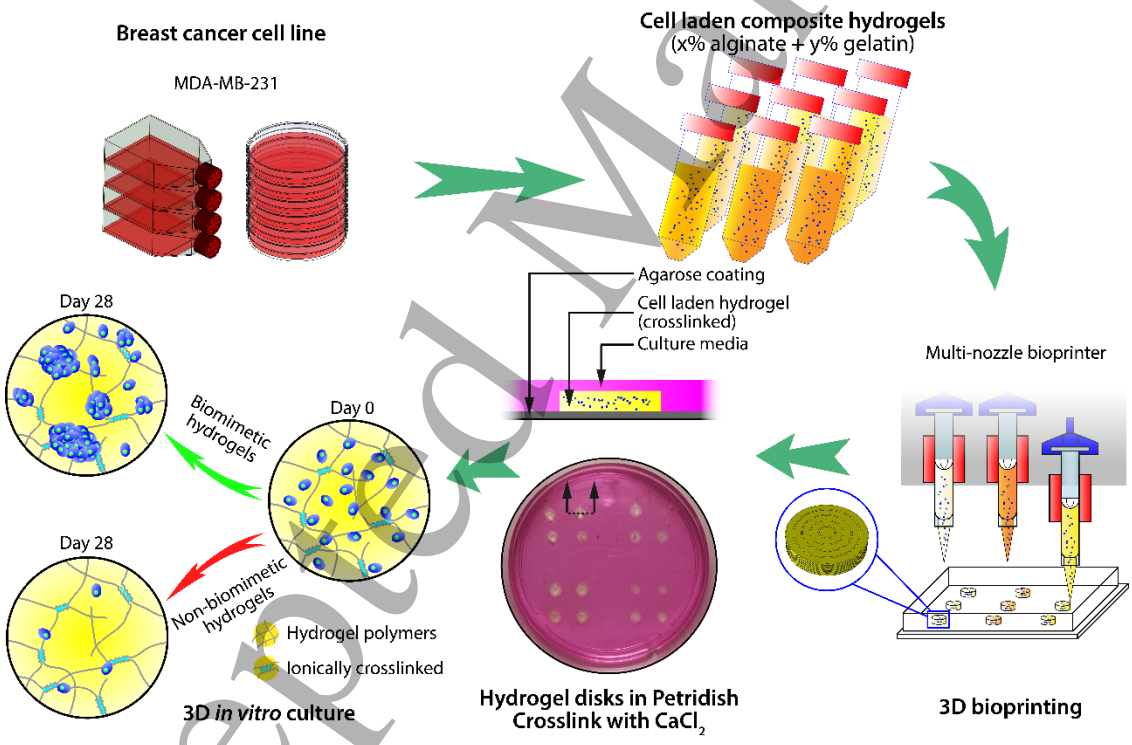

Figure 1. Schematic depicting the generation of the composite gels, bioprinting process, and subsequent generation of MCTS of breast cancer cells in bioprinted alginate/gelatin hydrogels.

Despite both alginate and gelatin having been used in cancer studies, limited work has been done to relate the initial concentrations of each constituent while evaluating the final morphologies and

behaviors of cancer cells. In one of our previous publications, we experimentally established a protocol to print and develop MCTS using a fixed ratio of alginate and gelatin concentrations[46]. However, in-depth studies of printability, post-printing elasticity, cell adhesion potential, and their influences on promoting MCTS are still poorly understood. Here we present a quantitative approach to evaluate cell reorganization into MCTS within bioprintable hydrogel composites comprised of differing weight percent (w%) of alginate and gelatin creating bioinks with tunable mechanical and cell-adhesion characteristics (**Figure 1**). MDA-MB-231 breast cancer cells show markedly different responses towards MCTS formation dependent upon the initial elasticity and cell-adhesion potential of the bioink. This study provides insight into the design and optimization of bioinks to generate MCTS with controllable growth rates, frequencies, and size.

2. MATERIALS AND METHODS

2.1. Material Preparation. Hydrogel solutions were prepared similarly to previously published protocols[46, 47]. Briefly, sodium alginate (Protanal LF 10/60 FT, FMC BioPolymer) and gelatin (bovine skin type B, G9391, Sigma-Aldrich) powders were dissolved in Dulbecco's phosphate buffered saline (DPBS, 1X, w/o Calcium, w/o Magnesium, sterile, pH 7.2 Gibco) using magnetic stirring at 60 °C for 1 hour; followed by continuous mixing for three hours at room temperature (RT). The final alginate concentrations in the precursors were 1, 3, or 5%; and gelatin concentrations were 5, 7, or 9% (referred to as AxGy for *x*% alginate and *y*% gelatin). All hydrogel solutions were stored at 4 °C and used within one week. A 100 mM $CaCl_2$ alginate crosslinking solution was prepared by dissolving $CaCl_2$ (Sigma-Aldrich) into sterile ultrapure water (MilliQ) and stored at 4 °C.

2.2. Bioprintability Tests. The composite un-crosslinked hydrogels were heated to 37 ºC to melt the gelatin. Extrusion tests were performed using 3 cc cartridges with G27 conical nozzles

(EFD Nordson, USA) mounted onto a BioScaffolder 3.1 (GeSiM, Germany) bioprinter. Cuboid models ($10 \times 10 \times 1.5$ mm^3) with a mesh size of 1 mm and layer thickness of 150 μm were printed with pressure ranging between 50 kPa to 300 kPa to determine the minimum pressure required for smooth extrusion. The precursor is considered "printable" if it exhibits sufficient yield stress to prevent its collapse as well as smooth extrusion out of the nozzle such that no corrugation appears. If the extruded filament spreads out after extrusion, it indicates the material has insufficient yield stress to support its weight. Contrarily, if the extrudate shows apparent "peaks and valleys" along it, or breaks within one filament, it is considered too brittle and non-printable. The time frame within which the precursor shows printability is referred to as its "printing window".

The quality of printed structures was quantified by measuring the width variation along each filament. Specifically, 10 points were randomly chosen along each filament where the width across that point was measured. We introduce the normalized roughness (R_N) to quantify the smoothness of filaments, which is defined by the ratio of the standard derivation of widths to mean width:

$$R_N = \frac{SD(w_i)}{\overline{w}} \times 100\% = \frac{\sqrt{\frac{\sum_{i=1}^{N}(w_i - \overline{w})^2}{N-1}}}{\overline{w}} \times 100\% \quad (1)$$

where $\overline{w}$ is the mean width of a filament, $N = 10$ is the data points collected, and w_i is the width measured at each point. Smoother filaments (better quality) result in smaller R_N ($R_N = 0$ for perfectly smooth line), while corrugated, shark-skinned or discontinuous filaments result in larger R_N. The R_N numbers were measured for the filaments extruded at the earliest printable time for each composition of the precursor.

2.3. Rheological Measurements. All rheological tests were performed using an MCR302 rheometer (Anton Paar, Canada) with a Φ25 mm parallel measuring tool (PP25). An amplitude sweep was initially performed to measure the critical linear strain γ_c. A*x*G*y* precursors were sealed

under the measuring tool at 37 °C before the temperature was immediately decreased to RT and maintained at RT for 2 hours to simulate the gelling process. Next, the shear strain was ramped logarithmically from 0.01% to 100% at both 0.01Hz and 100 Hz. The region where both G', G" maintain a plateau is considered the linear-viscoelastic region (LVER), and the strain over which G' starts to decrease is the yield strain. γ_c was determined as 1/10 of the ultimate linear strain to ensure time sweeps were conducted within the material's linear elastic regime.

After the γ_c was obtained, isothermal time sweeps were conducted to study the gelation kinetics of the A*x*G*y* precursors. The precursor was loaded under the measuring tool, and the temperature was immediately decreased from 37 °C to RT. While the precursor underwent physical gelling, a sinusoidal strain of γ_c at 1 Hz was applied for a 2-hour period. G', G" and |η*| were recorded at one-minute intervals to measure the property change during the gelling process. To quantitatively understand the gelation process, the G'-time curves were fitted into the exponential formula to find time constants:

$$G(t) = G_\infty \left(1 - e^{-\frac{t}{\tau_c}}\right) \quad (2)$$

where G_∞ and τ_c are theoretical final storage moduli and time constants. The goodness of fitting was realized by calculating the Degree of Freedom Adjusted R-Square (R^2_{adj}) and Root Mean Squared Error (RMSE). Time constants were compared between different compositions.

Another series of amplitude sweeps were implemented to further understand the yielding properties of A*x*G*y* at different time points during gelation. Similarly, A*x*G*y* precursors were loaded onto the rheometer and allowed to gel at RT. This time, the oscillatory strain was applied logarithmically from 10% to 1000% at an angular frequency of 1 Hz at 10, 20, 30, 45, 60, 90 and 120 min following the initial gelling, and the G' and G" were recorded. When yielding happens, G' shows a decreased value and eventually crosses over G", indicating the sample transits from

solid-dominant to liquid-dominant appearance. The stress at the yield strain was considered the yield stress τ_y.

2.4. Relation between yield stress and minimum extrusion pressure. To relate the yield stress to the minimum extrusion pressure in printing tests, we plotted the minimum extrusion pressure *versus* yield stress at the different time of gelling for all AxGy samples. The boundary conditions were set at two extreme flow scenarios: the upper boundary assumes completely non-slippery at the wall of the nozzle (lubrication condition), while the lower bound assumes a perfectly smooth (slippery) wall of the nozzle. The upper bound was taken from the modified Cogswell's equation[48]:

$$P_{Cogswell} = \frac{2\tau_y}{\tan\alpha}\ln\frac{R_0}{R_1} \tag{3}$$

where $P_{Cogswell}$ is the minimum extrusion pressure, τ_y is the material's yield stress, α is the half-cone angle of the conical nozzle, and R_0, R_1 are the radius of the inlet and outlet of the nozzle. The power-law fluid model in Cogswell's original work is replaced by the Herschel-Bulkley model. The flowrate is set to zero to obtain the minimum pressure to initiate flow.

The lower bound was taken from the modified Snelling's equation[49] or Basterfield's equation[50]:

$$P_{Snelling} = 4\tau_y \ln\frac{R_0}{R_1} \tag{4}$$

$$P_{Basterfield} = 2\sqrt{3}\tau_y \ln\frac{R_0}{R_1} \tag{5}$$

In both Snelling's equation and Basterfield's equation, the wall of the nozzle is assumed to be completely slippery such that no shear effects are taken into consideration. In both criteria, the material is assumed to be isotropic, the difference between the two is Snelling's work used Tresca yield criterion while Basterfield's work used Von Mises yield criterion to calculate the maximal

shear stress. The Tresca yield criterion is also known as maximum shear stress criterion and it is trivial to calculate ($\sigma_{rr} - \sigma_{\theta\theta} = 2\tau_{max}$), where σ_{rr} and $\sigma_{\theta\theta}$ are the principle stresses at the radial and tangential direction, while it can be conservative and overestimate the pressure required for lower boundary. On the other hand, Von Mises yield criterion uses the maximal distortion energy to judge whether a material yields, which is relatively more complicated but has been proved a more accurate description of yielding behaviors ($\tau_{max} = \sqrt{\frac{1}{2}\boldsymbol{s}_{ij}\boldsymbol{s}_{ij}}$), where $\boldsymbol{s_{ij}}$ are the components in deviatoric stress tensor. One may note that the resultant formulae only differ by a coefficient that is close to each other (4 *versus* $2\sqrt{3}$), which indicates a similar estimation using either of the yield criteria.

For a given type of nozzle, all the three equations suggest a linear relation between the minimum extrusion pressure and material's yield stress. The only difference is the coefficient, which is dependent on the material and the nozzle geometry. We assume a linear relation for AxGy precursors and Gauge 27 conical nozzle used in our tests:

$$\hat{P} = \lambda\widehat{\tau_y} \tag{6}$$

where $\hat{P}$ and $\widehat{\tau_y}$ are the estimated pressure and yield stress, and λ is the slop coefficient. Linear regression was performed on collected pressure – yield stress data to find λ. The goodness of fitting was realized by calculating the Degree of Freedom Adjusted R-Square (R^2_{adj}).

2.5. Cell Preparation. GFP transfected (nuclei label) MDA-MB-231 breast cancer cell lines were cultured at 5% CO_2, 37 °C in DMEM medium (Gibco) at pH 7.2 supplemented with 10% fetal bovine serum (Wisent Bioproducts), 100 U/mL penicillin, 100 μg/mL streptomycin, and 0.25 μg/mL, amphotericin B (Sigma), in T-150 flasks (Corning). Cells were harvested with trypsin-EDTA (0.25%, 1×, Gibco) prior to bioprinting.

2.6. Model Fabrication. Precursor gels were first liquefied by warming to 37 °C to create homogeneous solutions. Upon usage, 1 mL of each type of precursor was loaded into a 3 cc cartridge; then, MDA-MB-231 cell suspension was injected into the precursor and mixed to make a final cell concentration of 1.0×10^6 cells/mL. The cell-laden precursors were kept at RT to allow gelation. When the printing window was reached, quadruplicate disk models ($\Phi 5 \times 1$ mm^3) per each type of precursor were printed using the pressures found in printability tests. For example, the cell-laden A3G7 precursor was printed after 20 min of gelation at RT with 70 kPa of extrusion pressure (refer to the Results section for more details). The disk model was made up of 5 concentric circle paths and 7 layers vertically. After printing, 100 mM $CaCl_2$ solution was added to the disks to crosslink the alginate and incubated at RT for 8 min. The disk models were then rinsed with DPBS twice, transferred to agarose-coated Petri-dishes, and cultured at 37 °C with 5% CO_2.

2.7. Microindentation. Cell-free disk samples with different compositions were mold casted, crosslinked, and kept within an incubator at 37 °C for 24 hours. Samples were then indented while maintained at 37 °C. A spherical indenter probe (radius 500 μm, made of stainless steel) was mounted onto a load cell (S-256, Strain Measurement Instrument, USA) and connected to a micro-manipulator (MP-285, Sutter Instrument Co., USA). Force-displacement data was acquired, and the unloading curve was extracted to calculate the apparent Young's modulus. For soft biological materials, the adhesion between the sample and the indenter can require addition work to separate them. Hence, the JKR adhesive indentation model was used as a modified Hertzian model to account for the adhesive effects[51, 52]:

$$F = \frac{4}{3} \cdot \frac{E_s}{1-\nu^2} \cdot \frac{a^3}{R} - \sqrt{8\pi a^3 \cdot \frac{E_s}{1-\nu^2} \cdot \gamma} \quad (7)$$

$$\delta = \frac{a^2}{R} - \sqrt{\frac{2\pi a(1-\nu^2)\gamma}{E_s}} \quad (8)$$

where F is the load, E_s is the effective elastic modulus (also the apparent Young's modulus), ν is the Poisson ratio, R is the probe radius, a is the contact radius, γ is the surface tension of the sample, δ is the indentation depth (deduced by $\delta=D-\Delta F/K_c$), D is the translational movement of the micro-manipulator between the maximal loading and detaching position on the unloading curve, and K_c is the spring constant of load cell.

For water-rich hydrogels, the surface tension of water can be used as an approximation of that of the hydrogel[53, 54], and thus γ is set to be 70.0mJ/m^2. Note that when the surface tension is omitted ($\gamma = 0$), formulae (7) and (8) reduce to the original Hertzian Model[51]. Due to the high water content, the hydrogels can also be regarded as incompressible materials ($\nu = 0.5$). For the convenience of data fitting, formulae (7) and (8) can be organized into one formula:for an incompressible material,

$$\frac{1}{R}\left\{\frac{9RF}{16}\cdot\Lambda\right\}^{\frac{2}{3}} - \left(\frac{3\pi\gamma}{2}\right)^{\frac{1}{2}}\cdot\left\{\frac{9RF}{16}\cdot\Lambda\right\}^{\frac{1}{6}} = (E_s)^{\frac{2}{3}}\cdot\delta \quad (9)$$

where $\Lambda = 1 + \frac{3\pi R\gamma}{F} + \sqrt{2\cdot\frac{3\pi R\gamma}{F} + \left(\frac{3\pi R\gamma}{F}\right)^2}$. The left hand side of (9) is a function of force, and the right hand side is a function of indentation depth. The force-indentation data can be fitted into (9) to obtain the Young's modulus E_s.

2.8. Confocal Microscopy. Confocal microscopy (Olympus IX83, Olympus Life Science) was used to observe cell morphology and formation of MCTS. At each observation position, a Z-stack scan (500 μm thickness) was implemented with 20 and 10 μm steps, at magnifications of ×4 and ×10. MCTS volume was estimated using representative z-stack images from the center of each disk, 3D maximum filter was applied to the stacks, and the background noise was removed based

on "rolling ball" algorithm (50-500 pixels depending on MCTS size) using Fiji software[55-57]. Regions of interest containing MCTS were manually segmented using segmentation editor Fiji plugin. Finally, 3D object counter was used to calculate the volume of the individual MCTS[58]. We classified the MCTSs into three categories: small (15,000–200,000 μm^3), medium (200,000–700,000 μm^3), and large (>700,000 μm^3), which fit the sizes reported in the literature[59-61].

For 3D reconstruction, unlabeled MDA-MD-231 MCTSs grown in A1G7 or A3G7 were stained with Hoesch 33342 (nucleus, Tocris Bioscience) and Alexa Fluor® 633 phalloidin (actin, ThermoFisher Scientific), respectively, following manufacturer's instructions. Confocal images were acquired with Nikon A1+ confocal microscope, a Z-stack scan (200 μm thickness) of 1μm step and a ×20 magnification was used. Brightness, contrast and channel split of each Z-stack were adjusted using Fiji software. For 3D modeling, each channel was loaded to open source application MorphoGraphX[62] in order to acquire top, front and full 3D views of MCTS in hydrogels.

2D reconstruction was also performed by image projection with maximal intensity. The threshold was set to highlight fluorescent signals, and cell/spheroid number, area ratio as well as the fluorescent intensity was quantitatively analyzed with the built-in "Analyze Particle" function of Fiji. The relative fluorescent intensity and the area ratio were deduced by normalizing total fluorescent intensity/area ratio to those of Day 0.

MCTSs viability was determined using calcein-AM (AAT Bioquest, Inc) and ethidium homodimer-1 (EthD-1, Biotium) assay. Calcein-AM is a cell-permeant component that enters the cells and is cleaved by esterases inside the living cells, producing an intense green fluorescence (excitation/emission ≈495/515 nm); while EthD-1 enters cells with damaged membranes and then bind to nucleic acids generating a bright red fluorescence in dead cells (excitation/emission ≈495/635 nm)[63]. Unlabeled MDA-MD-231 cells were grown into A1G7 or A3G7 for 28 days;

each 7 days, samples were taken from cultures and incubated with calcein-AM/EthD-1 (2μM/4μM) solution in DPBS at 37°C during 45 min, following by confocal imaging acquisition using a Z-stack scan (500 μm thickness) with 10 μm steps and ×4 magnification. Images were processed as 2D reconstruction above mentioned. The fluorescent intensity was normalized to Day 0.

2.9. Statistical Analysis. All test samples were triplicated unless stated otherwise. Data were plotted using Prism 7 (GraphPad Software Inc., USA). Data are presented as Mean ± SD. Where comparisons were made, One- and Two-ways ANOVA and Tukey's and Bonferroni's *post-hoc* test were used with $P < 0.05$ considered significant. Volume data were plotted as box plot graphs using OriginPro 9 software, with a box limit of 25th and 75th percentiles and a minimum-maximum whisker's range.

3. RESULTS

3.1 Rheological Characterization. When the summation of alginate and gelatin concentrations remains the same, their gelation curves follow a similar pattern, *viz*., for any AxGy precursors, as long as *(x + y)* are the same, their gelation curves show a similar pattern and time constants (**Figure S1**). For instance, A1G9, A3G7, and A5G5 all have *(x + y = 10)*, and their fitted G'-time curves give time constants of 24.35 min, 26.46 min, and 30. 77 min, respectively. This indicates that the precursors with the same total polymer concentration start to stabilize at almost the same time of gelling. For those with the same *(x + y)*, the absolute values of their G' and G" unexceptionally increase with gelatin concentrations (**Figure S2**).

Moreover, increasing either the alginate or gelatin concentration increases the complex viscosity, which subsequently leads to a higher resistance to flow (**Figure 2 (b), Figure S3 (d-f), Figure S4 (d-f), Table S1-S2**) thus resulting in lower flow rates.

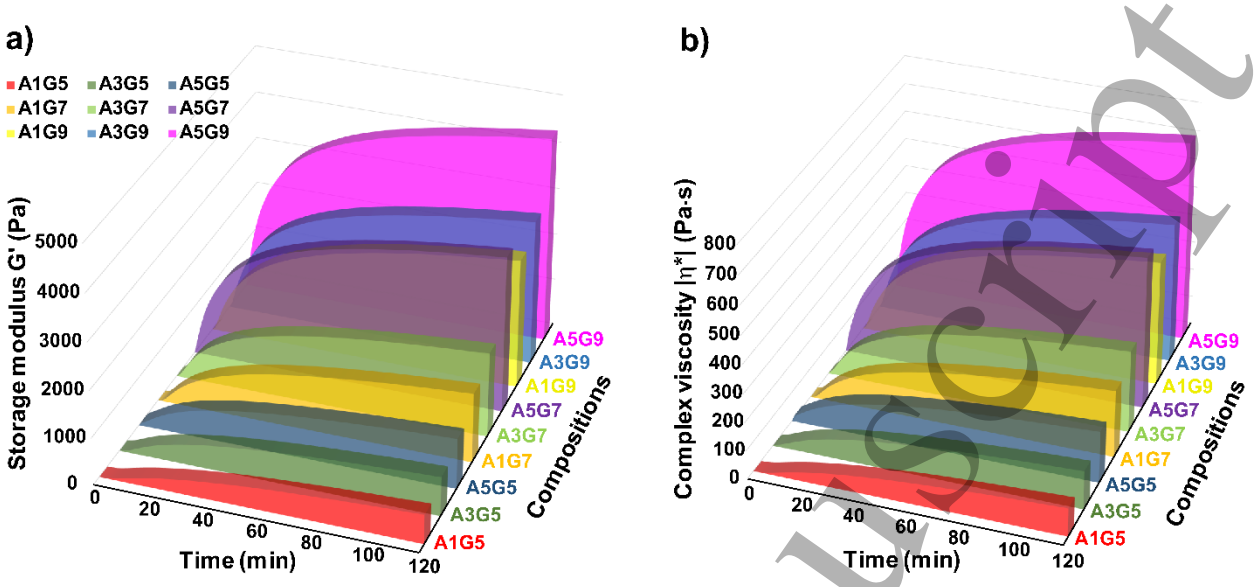

Figure 2. Gelation kinetics of AxGy hydrogel precursors. (a) shows storage modulus (G') versus gelation time for different compositions. (b) shows complex viscosity (η*) versus gelation time for different compositions.

The yield stress of AxGy increases during the gelation process (**Figure S5**). Surprisingly, even the softest precursor, A1G5, has a yield stress of 26.3 ± 8.5 Pa at 10 min of gelation in rheological tests, regardless of a liquid state in the actual printing test. This discrepancy can be attributed to the extensive time for heat dissipation of the precursors sealed in the cartridge *versus* a rapid thermal equilibrium in rheological tests (further discussed in the next section).

3.2. Bioprintability of AxGy precursors. All the compositions of AxGy can be printed at different initial time points using the corresponding minimum pressures (**Figure 3 (b)**). In all of the A*x*G*y* hydrogel precursors, the printing window remains similar for samples with the same *(x + y)* values (**Figure 3 (b)**).

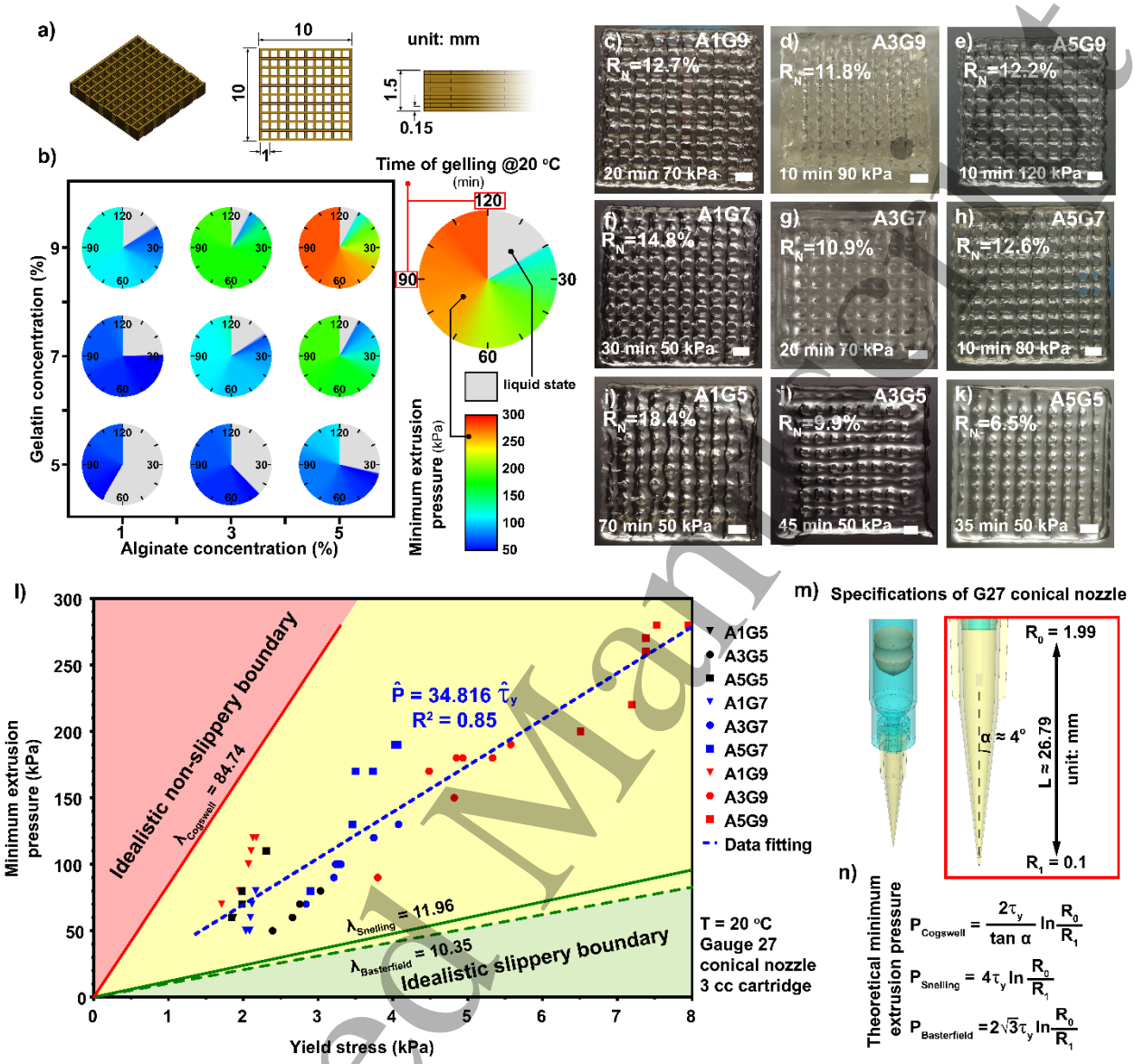

Figure 3. Printability of hydrogel precursors. (a) CAD of printed mesh model (unit: mm). (b) shows printing windows of precursors with different alginate and gelatin concentrations. Each round panel inside the plot represents one type of AxGy precursors. The numbers on the perimeter of the panel represent the time of gelling (min) before the printing. The color bar indicates the minimum pressure required to extrude the material using a G27 conical nozzle at RT. (c-k) demonstrate cuboid mesh models printed of AxGy. The time of gelling, extrusion pressure, and normalized roughness are shown for each printed mesh. Scale bar is 1 mm. (l) scatter plot of

minimum extrusion pressure *versus* yield stress. The solid red line is the upper bound defined by equation (3), the solid green line and dashed green line are lower bounds defined by equation (4) and (5). Blue dashed line represents a linear regression, with the estimated equation and goodness of the fitting. (m) shows the geometric parameters of a Gauge 27 conical nozzle. (n) shows the explicit formulas of the boundary conditions.

The minimum extrusion pressure is linearly related to the precursor's yield stress. The applied pressure imposes a stress on the material, which needs to exceed the material's yield stress to initiate flow. The pressure – yield stress data fitting gives a linear coefficient $\lambda = 34.816$, such that:

$$\hat{P} = 34.816\widehat{\tau_y} \tag{10}$$

with $R^2_{adj} = 0.85$. All the AxGy precursors, at all the tested time of printing follow this linear trend when extruding through G27 conical nozzles. The fitted curve lies within the upper bound defined by eq. (3) (idealistically non-slippery wall), and the lower bound defined by eq. (4) and eq. (5) (idealistically slippery wall), suggesting the AxGy precursors are partially slipping at the wall of the G27 conical nozzles (**Figure 3 (l)**). Note the G27 nozzle has an outlet radius of 0.1 mm (dimensions shown in **Figure 3 (m)**), which satisfies most of our printing work. For other types of nozzles, the boundary conditions can be calculated similarly using eq. (3~5).

All the precursors exhibit yield stresses even at 10 min of gelling in rheological tests when they are still in a liquid form in printing tests and cannot be printed. The yield stress values obtained before the earliest printable time are thus discarded in the data fitting process. One possible reason of the discrepancy is that in the rheological tests the temperature is immediately decreased from 37 °C to RT such that the precursors undergo quenching processes, while in printing tests the

precursors anneal to RT leading to a discrepancy to the rheological results. Thus, the yield stresses obtained in rheological tests can be over-estimated values.

The time constants separate the gelation process into a rapid gelling regime and a slow reinforcing regime. During the rapid gelling regime, one needs to rapidly increase extrusion pressure to successfully extrude the material, while in the slow reinforcing regime, fewer changes are needed regarding the required extrusion pressure. Noteworthy, the time constant for A1G5 is 57.58 min, which happens before its earliest printable time (70 min). Thus, A1G5's printability is maintained throughout the printing session (from 70 min to 120 min) without a noticeable increase in the required extrusion pressure. Similar behaviors are shown by A3G5 and A5G5.

The meshes were printed at the earliest time in the printing window of a precursor using the minimal extrusion pressure possible. Before the printing window, the material is too fluid, and adjacent filaments fuse into each other. When using a pressure below the minimum required pressure, extrusion is unstable, and clogging within the nozzle frequently occurs. All of the printed examples shown in **Figure 3 (c-k)** exhibit post-printing stability, suggesting sufficient yield stress to support the structure.

Most of the printed filaments show a normalized roughness of ~10%, while the worst is A1G5 (~18.4%) and the best is A5G5 (~6.5%). Intriguingly, AxG5 series as the "slowest" gelation precursors, cover both the best and the worst printing qualities, which implies a low gelatin concentration may lead to unstable extrusion behaviors (further explained in the Discussion section). All the other AxGy precursors show similar normalized roughness numbers ranging from 10.9% to 14.8%. The relatively small normalized roughness numbers exhibit a satisfying surface quality of the extruded structures.

3.3 Elasticity of crosslinked hydrogels. The Apparent Young's modulus (E_s) of the different formulations can be tuned between 5.46 to 22.88 kPa (**Figure 4**) dependent upon the w% alginate, (e.g., 1% alginate results in E_s between 5.46 – 7.92 kPa; whereas 3% alginate has an E_s between 13.30 - 16.31 kPa; and 5% alginate results in an E_s between 19.90 - 22.88 kPa). Among the samples with the same alginate concentration, gelatin does not play a noteworthy effect on E_s as the gelatin within the composite exists in a liquid phase at 37°C.

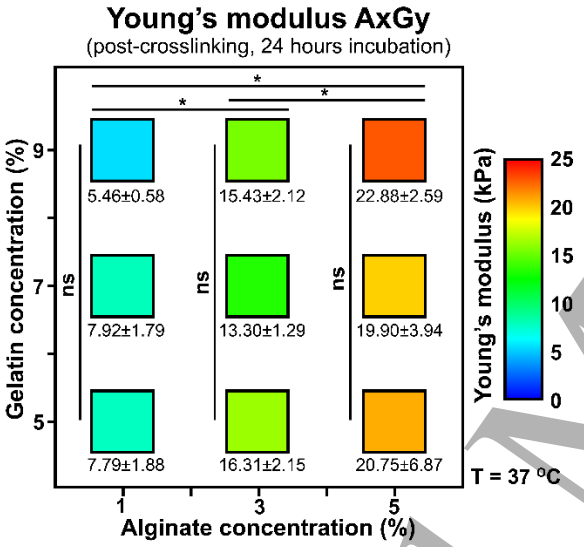

Figure 4. Apparent Young's Modulus measured 24 hours after crosslinking by micro-indentation. Plotted with the concentrations of gelatin and alginate on vertical and horizontal axes, and color bar represents the values of apparent Young's modulus. Asterisks (*) represent a significant difference between two groups, calculated by pooling all the data for the different gelatin concentrations, with $P < 0.05$, n=10. "ns" means non-significant difference.

3.4 Generation of MCTS in hydrogels. In general, the softer hydrogels have higher chances to induce MCTS. All of the A1Gy samples induce MCTS formation starting on day 7 of culture and continue to grow in size until experiments were ceased on day 28. Among the A1Gy samples, A1G7 and A1G9 result in both larger and more rapid MCTS generation in comparison to A1G5

bioinks that contain fewer cell-adhesive gelatin molecules (**Figure S6**). MDA-MB-231 cells grown in A3Gy gels result in a less frequent formation of MCTS and smaller MCTS sizes on day 7, with a decreasing trend in resulting MCTS after day 14 (**Figure S7**). In A5Gy samples, MDA-MB-231 cells remained as single populations, with cell numbers decreasing more rapidly than those printed using A3Gy composite gels (**Figure S8**).

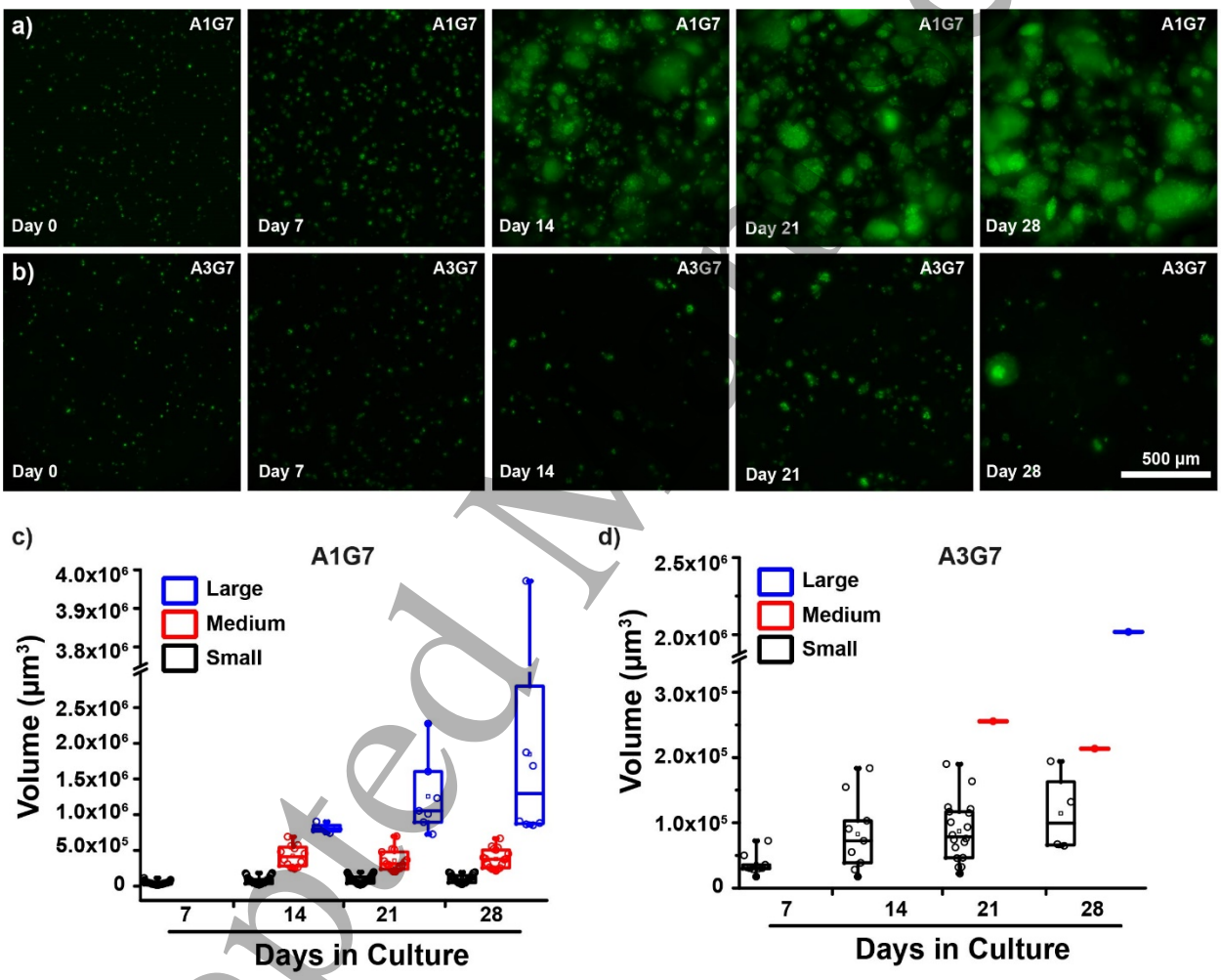

Figure 5. Confocal images of bioprinted A1G7 and A3G7 disks and quantitative analysis of MCTS in a 28-day period. Row (a) and (b) show the morphological MCTS variation by time in A1G7 and A3G7, respectively. Magnification ×10. Images (c) shows the volume of each spheroid in a representative A1G7 sample during 28 days of culture, with categories of small (15,000–200,000 μm^3), medium (200,000–700,000 μm^3), and large (>700,000 μm^3) MCTS presented in black, red

and blue color. (d) shows the same data for A3G7, with the same thresholds in categorization. Box plot graphs were plotted using a box limit of 25th and 75th percentiles with a minimum-maximum whisker's range.

3.5 Development of MCTS. Among the hydrogels that induce MCTS, softer ones cause earlier onset of medium to large sized MCTS and higher total MCTS numbers. Here we perform qualitative comparisons of MCTS development in A1G7 (**Figure S6 (b)**, E_s = 7.92 ± 1.79 kPa) and A3G7 (**Figure S7 (b)**, E_s = 13.30 ± 1.29 kPa) hydrogels. A1G7 gels promote the formation of medium and large MCTS after 14 days of culture (**Figure 5 (a, c)**), while A3G7 produced medium MCTS after 14 days with large MCTS forming only at day 28 (**Figure 5 (b, d)**). The number of small and medium size MCTS/mm^3 in A1G7 and A3G7 samples show significant differences, producing more MCTS in A1G7 compare with A3G7 after 7 days of culture (**Figure S9 (a, b)**). For large-size spheroids, A1G7 shows a significant higher quantity of MCTS that A3G7 after 14 days of culture (**Figure S9 (c)**). The largest volume for MCTS found in A1G7 and A3G7 hydrogels are ≈ 3,971,137 μm^3 and ≈ 2,017,647μm^3, respectively, on day 28 of culture.

To evaluate the status of MCTSs in A1G7 or A3G7, we perform viability test. Cells and MCTSs growing in A1G7 shows high proliferation rate (**Figure 6 (a)**) through time, while MCTSs in A3G7 keeps the same proliferation rate compared with day 0. The confocal images (**Figure 6 (b, c)**) confirm the previous results on MCTS sizes (**Figure 5**), where MDA-MB-231 cultured into A1G7 presents more and larger MCTS compared with A3G7. Regarding to MCTSs viability, both A1G7 and A3G7 cultures show high viability (**Figure 6 (b, c)**).

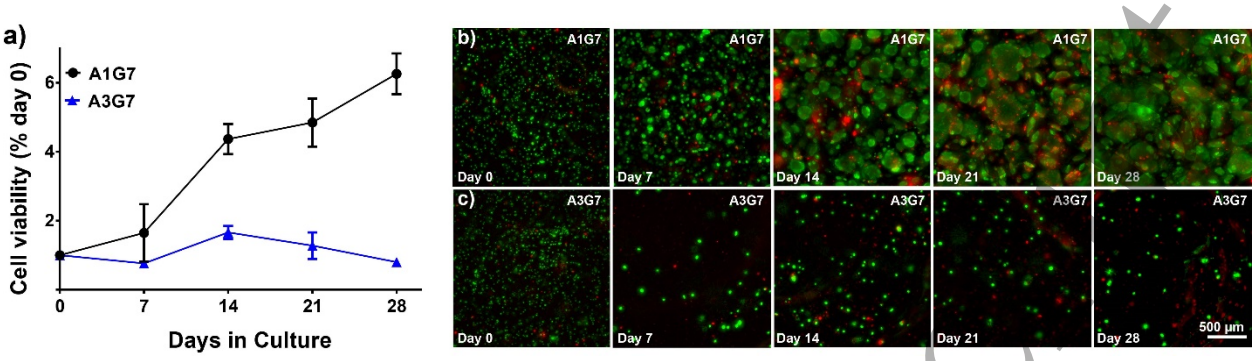

Figure 6. MDA-MB-231 cell viability during 28 days of culture within A1G7 or A3G7 hydrogels. (a) the viability of single cells as well as MCTS was determined each 7 days and normalized against day 0. Data presented as Mean ± SD, n≥3. Confocal images of live (green) and dead (red) MCTS in A1G7 (b) and A3G7 (c). Magnification ×4, scale bar 500 μm.

High magnification 3D reconstruction confirms the distribution, volumes, and morphologies of the MCTS formed in A1G7 and A3G7 at 21 days of culture (**Figure 7**), where A1G7 allows the production of large MCTS (**Figure 7 (a, b)**) compared with A3G7 (**Figure 7 (c, d)**).

The modulus dependency of MCTS development can also be presented by the normalized fluorescent intensity and the surface area of 2D projected confocal images. The measured fluorescent intensities of A3Gy (E_s range from 13.30 to 16.31 kPa) and A5Gy samples (E_s range from 19.90 to 22.88 kPa) decrease by days of culture (**Figure S10(a)** triangles and circles, respectively), and are considerably lower than the A1Gy counterparts (E_s range from 5.46 to 7.92 kPa). MCTS growth in samples cultured in the A5Gy gels exhibits slightly lower (yet non-significantly different) fluorescent intensities (0.3 times to Day 0) than that in A3Gy samples (0.5 times to Day 0) (**Figure S10(a)**, circles *versus* triangles). A similar trend can be observed via comparisons of the normalized surface area ratio (**Figure S10 (b)**).

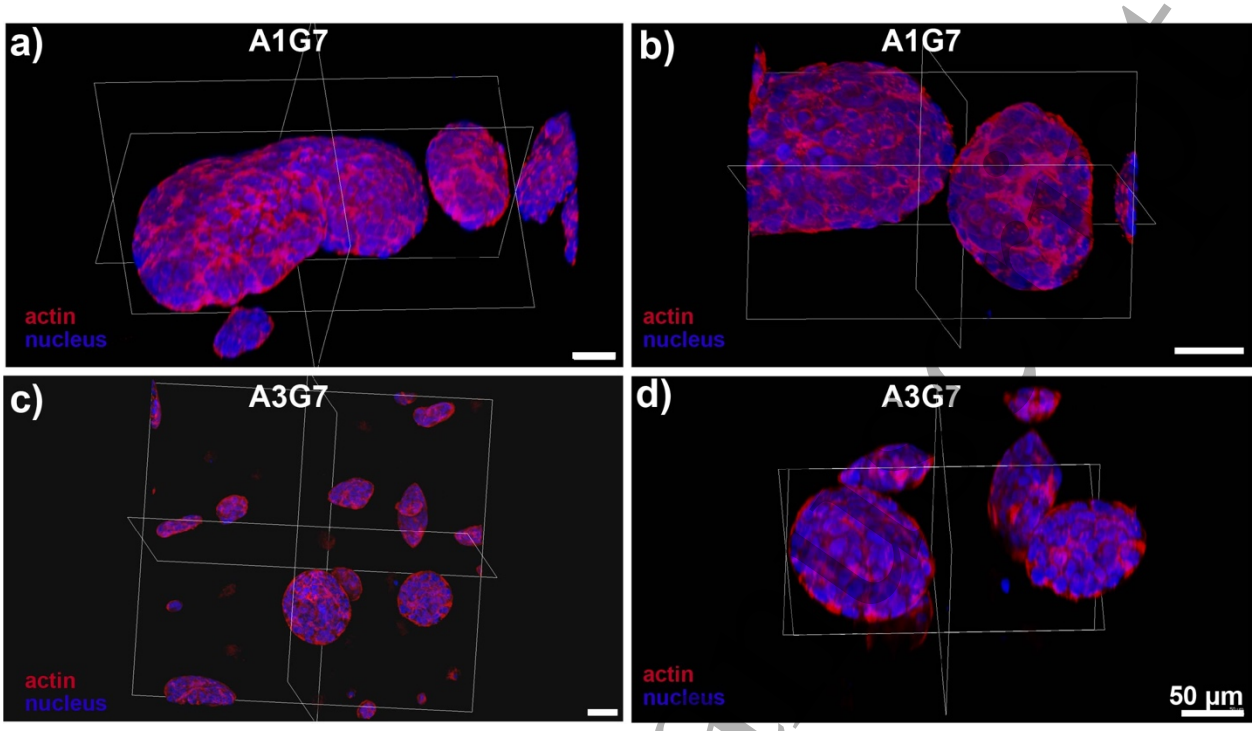

Figure 7. 3D reconstruction of MCTS showing the representative morphologies and sizes of MCTS formed in A1G7 (a, b) and A3G7 (c, d) hydrogels after 21 days of culture. A zoom in of the MCTS is presented in b) and d), displaying the actin organization in the spheroids. Magnification ×20, scale bar 50 μm.

In A1Gy series, a higher gelatin portion results in a higher normalized fluorescent intensity and surface area. For example, in the A1G9 gels the intensity on Day 28 increases to 2.4 times than that on Day 0, while the same ratio for A1G5 is 1.5 times (**Figure S10 (a)**, squares). This trend cannot be observed in A3Gy and A5Gy series, presumably due to the over-stiff network inhibiting MCTS development.

Noticeably, the A3Gy and A5G5 samples see a short-term increase of normalized fluorescent intensity and surface area on Day 7 followed by a continuous decrease until Day 28 (**Figure S10 (a, b)**), indicating the short-term studies of cell behavior is insufficient to describe the biocompatibility and bioactivity of the biomaterial in the long-term.

4. DISCUSSION

Our results demonstrate the effect of bioink composition on both the bioprintability and formation of MDA-MB-231 MTCS. Printability of a material primarily depends on two aspects: the material's intrinsic properties (such as modulus, yield stress, viscosity, thixotropic recovery *et cetera*) and the external conditions (such as applied pressure, nozzle geometry, cartridge size *et cetera*).[64-67] Soft materials with similar rheological properties are highly likely to achieve similar printability. In our experiments, A*x*G*y* with the same sum of *(x + y)* w/v% ratio values generally exhibits similar printing windows. In gelatin-rich composites, a small fraction of alginate is needed to achieve a similar printing window with alginate-rich, gelatin-less composites, and *vice versa*. This is due to the samples having the same water w/v% of their content and therefore exhibit similar rheological properties. Therefore, it provides the possibility to create hydrogels with similar printability but completely different mechanical/biological properties after crosslinking and during culturing (i.e., A1G7 vs. A3G5).

Yield stress can influence the startup pressure required for extrusion as the applied stress should exceed the yield stress such that the material enters the plastic deformation regime, and macroscopically, starts to flow[68-70]. In our experiments, a linear relation was found between the minimum extrusion pressure and the material's yield stress, which provides a general guide for bioprinting regardless of the formulation of material. As long as the yield stress is known, the minimum extrusion pressure can be estimated. When the pressure exceeds the minimum pressure, the additional stress exerted on the material leads to an increased flow rate.

Another important contribution brought by yield stress is the post-extrusion structural stability. A material with yield stress can withstand its weight against gravity, while a liquid that has little

to no yield stress collapses under gravity. The AxGy hydrogels gain sufficient yield stress as they physically gel at RT, such that the printed meshes retain their structures without spreading out.

The AxG5 series is unique as the 5% gelatin tends to recover slowly after violent shear, which delays the printing window by ~10 min after the time constants. Actually, in AxG5 hydrogels, the alginate composite tends to manifestly influence the printing quality. When alginate concentration is high, the printed structure may "collapse" slower, which gives sufficient time for the 5% gelatin to rebuild the yield stress post-extrusion and thus resulting in lower R_N. On the other hand, the alginate-less A1G5 has neither rapid recovery (due to low gelatin %) nor slowed flowing (due to low alginate %), and eventually results in higher R_N.

Factors such as material composition, matrix elasticity, cell concentration, and cancer cell type could affect the MCTS formation in 3D cultures[71]. With increased gelatin concentration, more adhesion sites are provided enhancing the potential for cell-matrix interactions. Consequently, cells printed in gels with greater gelatin concentration exhibit higher proliferation activities and therefore, develop into larger MCTS. Thus, the gelatin provides tunable biofunctionality to the hydrogel without noticeably altering the mechanical properties.

Samples in the A3G*y* and A5G*y* series, except for A3G7, do not facilitate MCTS formation/growth due to their high modulus and a dense molecular network which can inhibit cell morphology and movement. In general, tumors have a higher Young's modulus than normal tissue due to ECM crosslinking[72]. Since the migration, proliferation and MCTS formation inside of 3D environments is related with the matrix elasticity, a stiffer material could negatively affect the cells ability to migrate and proliferate inhibiting the formation of, or resulting in reduced size MTCS[72, 73]. This could explain why the A1G*y* hydrogels were better matrices for MCTS formation. It is well known that matrix elasticity plays a critical role in cancer cell viability,

formation and progression of tumors[71, 74, 75]. The effect of elasticity on cell function relies on the expression of proteins, such as integrins, and the downstream focal adhesion complex proteins, which are sensed and transduced into mechanical and biochemical signals in specific pathways[74]. The necrotic core occurs dependent upon MCTS size, which is correlated with cell function as well as drug penetration, and nutrient and oxygen transport. MCTSs with diameters ranging from 200 to 500 μm are large enough to develop chemical gradients, while MCTS >500 μm develop a central secondary necrosis where the inner cells die by apoptosis or necrosis. MCTS with diameters <150 μm are frequently used for drug testing, and may be sufficient to exhibit 3D cell-cell and cell-matrix interactions but are not large enough to exhibit oxygen gradients with hypoxic regions or proliferation gradients [23, 59, 76]. Almost all MCTSs formed in A1G7 and A3G7 are smaller than 2.0×10^6 μm^3 (≈150 μm); based on that, we think that oxygen and nutrients transport to the core of the MCTS is not limited or slightly limited (in larger MCTSs) but without negative effects on cells proliferation or necrotic core formation. The organization of actin stress fibers at the periphery of MCTS in both A1G7 and A3G7 could be correlated with the cell/MCTS proliferation and migration inside of the hydrogels[77-79].MDA-231 cancer cells encapsulated in PEGDA hydrogels with a Young's modulus of 5 kPa promote the formation of larger MCTS, higher cell and sphere density compared with PEGDA of ≤ 2kPa and ≥25kPa, suggesting that cells prefer a material ranging in this elasticity[71]. Both A1G*y* and A3G7 hydrogels promote the MCTS formation within 7 days of culture; however, A1G7 samples allow a greater quantity of medium and large MCTS size during culture compared to the A3G7 hydrogel samples. This could be due to matrix elasticity that affects the expression of mechanosensors and mechanotransduction complex proteins [71, 74, 75]. It is clear that more studies regarding molecular mechanisms must

be done in order to understand the complex biology behind of MCTS formation and cancer tumor progression.

5. CONCLUSIONS

Overall, the A1G7 and A1G9 samples have both high printability and biofunctionality, i.e., they reach their corresponding printing windows within 30 min and have been proven to have limited negative impacts on cell viability and proliferation. They also have minimal mechanical property changes over a considerably longer printing window and can provide enough adhesion sites for cells to attach, proliferate and aggregate. For all tested hydrogels, the minimum extrusion pressure during printing is linearly related to the material's yield stress, which is determined by formulations of the material. The elasticity of the crosslinked gel is solely determined by alginate concentrations, while the biological functionality is tuned by gelatin concentrations. Cancer cells show elasticity and formulation dependence on the production of spheroids with different volumes. These hydrogels allow the biofabrication of cell models that can be used to create 3D disease models with high-throughput, low cost, and high reproducibility as a viable alternative to 2D cell cultures and small animal models.

ASSOCIATED CONTENT

Supporting Information. The following files are available free of charge.

Figures S1 – S10, Tables T1, T2 (PDF)

AUTHOR INFORMATION

Corresponding Author

*Joseph M. Kinsella; joseph.kinsella@mcgill.ca

Author Contributions

‡Tao Jiang and ‡Jose Gil Munguia-Lopez contributed equally to this work. Tao Jiang developed composite hydrogels, conducted rheological experiments, micro-indentation, and bioprinting tests. Jose Gil Munguia-Lopez cultured cells, conducted viability tests, confocal microscopy, and developed methods to quantify spheroid size. Salvador Flores-Torres helped conduct bioprinting, confocal microscopy and spheroid size quantification. Kevin Gu, Maeva M. Bavoux, and Jacqueline Kort-Mascort helped conduct cell culture and confocal microscopy. Joel Grant and Sanahan Vijayakumar helped synthesize composite hydrogels. Allen J Ehrlicher contributed reagents and equipment, and expertise in rheology and biomaterials. Antonio De Leon-Rodriguez and Joseph M Kinsella provided supervision to all the work mentioned above. The manuscript was written through the contributions of all authors. All authors have approved the final version of the manuscript.

Notes

The authors declare no competing financial interest.

ACKNOWLEDGMENT

Tao Jiang thanks the China Scholarship Council (201403170354) and McGill Engineering Doctoral Award (90025) for the scholarship. Jose Gil Munguia-Lopez thanks CONACYT for scholarship funding (291168 and 291258) and FRQNT (258421). Salvador Flores Torres thanks CONACYT for scholarship funding (751540). Jacqueline Kort Mascort thanks CONACYT for scholarship funding (754427). Joseph M. Kinsella thanks the National Science and Engineering Research Council, the Canadian Foundation for Innovation, the Townshend-Lamarre Family Foundation, and McGill University for funding. Allen J Ehrlicher acknowledges NSERC

RGPIN/05843-2014 & EQPEQ/472339-2015, CIHR Grant # 143327, and CCS Grant #703930.

We would like to thank Prof Dan Nicolau for allowing us to use his confocal microscope, and Prof Morag Park for access to fluorescently labeled cell lines.

REFERENCES

[1] Ahmed E M 2015 Hydrogel: Preparation, characterization, and applications: A review *J Adv Res* **6** 105-21

[2] Ma Y, Lin M, Huang G, Li Y, Wang S, Bai G, Lu T J and Xu F 2018 3D Spatiotemporal Mechanical Microenvironment: A Hydrogel-Based Platform for Guiding Stem Cell Fate *Adv Mater* **30** e1705911

[3] Jiang T, Munguia-Lopez J G, Flores-Torres S, Kort-Mascort J and Kinsella J M 2019 Extrusion bioprinting of soft materials: An emerging technique for biological model fabrication *Applied Physics Reviews* **6**

[4] Huang G, Li F, Zhao X, Ma Y, Li Y, Lin M, Jin G, Lu T J, Genin G M and Xu F 2017 Functional and Biomimetic Materials for Engineering of the Three-Dimensional Cell Microenvironment *Chem Rev* **117** 12764-850

[5] Ma Y, Ji Y, Zhong T, Wan W, Yang Q, Li A, Zhang X and Lin M 2017 Bioprinting-Based PDLSC-ECM Screening for in Vivo Repair of Alveolar Bone Defect Using Cell-Laden, Injectable and Photocrosslinkable Hydrogels *ACS Biomaterials Science & Engineering* **3** 3534-45

[6] Ma Y, Ji Y, Huang G, Ling K, Zhang X and Xu F 2015 Bioprinting 3D cell-laden hydrogel microarray for screening human periodontal ligament stem cell response to extracellular matrix *Biofabrication* **7** 044105

[7] Tabriz A G, Hermida M A, Leslie N R and Shu W 2015 Three-dimensional bioprinting of complex cell laden alginate hydrogel structures *Biofabrication* **7** 045012

[8] Cuadros T R, Erices A A and Aguilera J M 2015 Porous matrix of calcium alginate/gelatin with enhanced properties as scaffold for cell culture *Journal of Mechanical Behaviors of Biomedical Materials* **46** 331-42

[9] Lee K Y and Mooney D J 2012 Alginate: properties and biomedical applications *Progress in Polymer Science* **37** 106-26

[10] Song W, Cao X and Wang Y 2016 3D Bioplotting of Gelatin/Alginate Scaffolds for Tissue Engineering: Influence of Crosslinking Degree and Pore Architecture on Physicochemical Properties *Journal of Materials Science & Technology* **32** 889-900

[11] Ouyang L, Yao R, Zhao Y and Sun W 2016 Effect of bioink properties on printability and cell viability for 3D bioplotting of embryonic stem cells *Biofabrication* **8** 035020

[12] Djabourov M, Leblond J and Papon P 1988 Gelation of aqueous gelatin solutions. I. Structural investigation *J. Phys. France* **49** 319-32

[13] Djabourov M, Leblond J and Papon P 1988 Gelation of aqueous gelatin solutions. II. Rheology of the sol-gel transition *J. Phys. France* **49** 333-43

[14] Rowley J A, Madlambayan G and Mooney D J 1999 Alginate hydrogels as synthetic extracellular matrix materials *Biomaterials* **20** 45-53

[15] Ouyang L, Yao R, Chen X, Na J and Sun W 2015 3D printing of HEK 293FT cell-laden hydrogel into macroporous constructs with high cell viability and normal biological functions *Biofabrication* **7** 015010
[16] Pathak A and Kumar S 2012 Independent regulation of tumor cell migration by matrix stiffness and confinement *Proceedings of the National Academy of Sciences of the United States of America* **109** 10334-9
[17] Stowers R S, Allen S C and Suggs L J 2015 Dynamic phototuning of 3D hydrogel stiffness *Proc Natl Acad Sci U S A* **112** 1953-8
[18] Soman P, Kelber J A, Lee J W, Wright T N, Vecchio K S, Klemke R L and Chen S 2012 Cancer cell migration within 3D layer-by-layer microfabricated photocrosslinked PEG scaffolds with tunable stiffness *Biomaterials* **33** 7064-70
[19] Chaudhuri O, Koshy S T, Branco da Cunha C, Shin J W, Verbeke C S, Allison K H and Mooney D J 2014 Extracellular matrix stiffness and composition jointly regulate the induction of malignant phenotypes in mammary epithelium *Nature Materials* **13** 970-8
[20] Fenner J, Stacer A C, Winterroth F, Johnson T D, Luker K E and Luker G D 2014 Macroscopic stiffness of breast tumors predicts metastasis *Scientific Reports* **4** 5512
[21] Cheng G, Tse J, Jain R K and Munn L L 2009 Micro-environmental mechanical stress controls tumor spheroid size and morphology by suppressing proliferation and inducing apoptosis in cancer cells *PLoS One* **4** e4632
[22] Zaman M H, Trapani L M, Sieminski A L, Mackellar D, Gong H, Kamm R D, Wells A, Lauffenburger D A and Matsudaira P 2006 Migration of tumor cells in 3D matrices is governed by matrix stiffness along with cell-matrix adhesion and proteolysis *Proceedings of the National Academy of Sciences of the United States of America* **103** 10889-94
[23] Hirschhaeuser F, Menne H, Dittfeld C, West J, Mueller-Klieser W and Kunz-Schughart L A 2010 Multicellular tumor spheroids: an underestimated tool is catching up again *J Biotechnol* **148** 3-15
[24] Lin R Z and Chang H Y 2008 Recent advances in three-dimensional multicellular spheroid culture for biomedical research *Biotechnol J* **3** 1172-84
[25] Hanahan D and Weinberg R A 2011 Hallmarks of cancer: the next generation *Cell* **144** 646-74
[26] Lee J M, Mhawech-Fauceglia P, Lee N, Parsanian L C, Lin Y G, Gayther S A and Lawrenson K 2013 A three-dimensional microenvironment alters protein expression and chemosensitivity of epithelial ovarian cancer cells in vitro *Laboratory Investigation* **93** 528-42
[27] Hickman J A, Graeser R, de Hoogt R, Vidic S, Brito C, Gutekunst M, van der Kuip H and Consortium I P 2014 Three-dimensional models of cancer for pharmacology and cancer cell biology: capturing tumor complexity in vitro/ex vivo *Biotechnology Journal* **9** 1115-28
[28] Fischbach C, Chen R, Matsumoto T, Schmelzle T, Brugge J S, Polverini P J and Mooney D J 2007 Engineering tumors with 3D scaffolds *Nature methods* **4** 855-60
[29] Faute M A d, Laurent L, Ploton D, Poupon M-F, Jardillier J-C and Bobichon H 2002 Distinctive alterations of invasiveness, drug resistance and cell–cell organization in 3D-cultures of MCF-7, a human breast cancer cell line, and its multidrug resistant variant *Clinical & Experimental Metastasis* **19** 161-7
[30] Mak M, Reinhart-King C A and Erickson D 2011 Microfabricated physical spatial gradients for investigating cell migration and invasion dynamics *PLoS One* **6** e20825

[31] Weigelt B, Ghajar C M and Bissell M J 2014 The need for complex 3D culture models to unravel novel pathways and identify accurate biomarkers in breast cancer *Advanced Drug Delivery Reviews* **69-70** 42-51
[32] Klinger R, Itasaki N, Welzel K, Owolabi F, Cummings B, Oconnor D, Saitoh S, Scholz D, Ivers L and Fujita Y 2014 Dynamic and influential interaction of cancer cells with normal epithelial cells in 3D culture *Cancer Cell International* **14** 1-16
[33] Fischbach C, Kong H J, Hsiong S X, Evangelista M B, Yuen W and Mooney D J 2009 Cancer cell angiogenic capability is regulated by 3D culture and integrin engagement *Proceedings of the National Academy of Sciences of the United States of America* **106** 399-404
[34] Edmondson R, Broglie J J, Adcock A F and Yang L 2014 Three-dimensional cell culture systems and their applications in drug discovery and cell-based biosensors *Assay Drug Dev Technol* **12** 207-18
[35] Hutmacher D W, Loessner D, Rizzi S, Kaplan D L, Mooney D J and Clements J A 2010 Can tissue engineering concepts advance tumor biology research? *Trends in Biotechnology* **28** 125-33
[36] Murali V S, Chang B J, Fiolka R, Danuser G, Cobanoglu M C and Welf E S 2019 An image-based assay to quantify changes in proliferation and viability upon drug treatment in 3D microenvironments *BMC Cancer* **19** 502
[37] Ling K, Huang G, Liu J, Zhang X, Ma Y, Lu T and Xu F 2015 Bioprinting-Based High-Throughput Fabrication of Three-Dimensional MCF-7 Human Breast Cancer Cellular Spheroids *Engineering* **1** 269-74
[38] Szot C S, Buchanan C F, Freeman J W and Rylander M N 2011 3D in vitro bioengineered tumors based on collagen I hydrogels *Biomaterials* **32** 7905-12
[39] Kenny P A, Lee G Y, Myers C A, Neve R M, Semeiks J R, Spellman P T, Lorenz K, Lee E H, Barcellos-Hoff M H, Petersen O W, Gray J W and Bissell M J 2007 The morphologies of breast cancer cell lines in three-dimensional assays correlate with their profiles of gene expression *Molecular oncology* **1** 84-96
[40] Grolman J M, Zhang D, Smith A M, Moore J S and Kilian K A 2015 Rapid 3D Extrusion of Synthetic Tumor Microenvironments *Advanced Materials* **27** 5512-7
[41] Fennema E, Rivron N, Rouwkema J, van Blitterswijk C and de Boer J 2013 Spheroid culture as a tool for creating 3D complex tissues *Trends in Biotechnology* **31** 108-15
[42] Peela N, Sam F S, Christenson W, Truong D, Watson A W, Mouneimne G, Ros R and Nikkhah M 2016 A three dimensional micropatterned tumor model for breast cancer cell migration studies *Biomaterials* **81** 72-83
[43] Huang T Q, Qu X, Liu J and Chen S 2014 3D printing of biomimetic microstructures for cancer cell migration *Biomedical Microdevices* **16** 127-32
[44] Zhao Y, Yao R, Ouyang L, Ding H, Zhang T, Zhang K, Cheng S and Sun W 2014 Three-dimensional printing of Hela cells for cervical tumor model in vitro *Biofabrication* **6** 035001
[45] Khavari A, Nyden M, Weitz D A and Ehrlicher A J 2016 Composite alginate gels for tunable cellular microenvironment mechanics *Sci Rep* **6** 30854
[46] Jiang T, Munguia-Lopez J, Flores-Torres S, Grant J, Vijayakumar S, De Leon-Rodriguez A and Kinsella J M 2018 Bioprintable Alginate/Gelatin Hydrogel 3D In Vitro Model Systems Induce Cell Spheroid Formation *J Vis Exp*

[47] Jiang T, Munguia-Lopez J G, Flores-Torres S, Grant J, Vijayakumar S, Leon-Rodriguez A and Kinsella J M 2017 Directing the Self-assembly of Tumour Spheroids by Bioprinting Cellular Heterogeneous Models within Alginate/Gelatin Hydrogels *Sci Rep* **7** 4575

[48] Cogswell F N 1972 Converging flow of polymer melts in extrusion dies *Polymer Engineering & Science* **12** 64-73

[49] Snelling G R and Lontz J F 1960 Mechanism of lubricant - extrusion of teflon tfe - tetrafluoroethylene resins *Journal of Applied Polymer Science* **3** 257-65

[50] Basterfield R A, Lawrence C J and Adams M J 2005 On the interpretation of orifice extrusion data for viscoplastic materials *Chemical Engineering Science* **60** 2599-607

[51] Johnson K L 1987 *Contact mechanics* (Cambridge [Cambridgeshire]; New York: Cambridge University Press)

[52] Argatov I and Mishuris G 2018 Indentation testing of biological materials. (Cham, Switzerland: Springer)

[53] Boujlel J and Coussot P 2013 Measuring the surface tension of yield stress fluids *Soft Matter* **9** 5898-908

[54] Luu L-H and Forterre Y 2009 Drop impact of yield-stress fluids *Journal of Fluid Mechanics* **632** 301

[55] Schindelin J, Arganda-Carreras I, Frise E, Kaynig V, Longair M, Pietzsch T, Preibisch S, Rueden C, Saalfeld S, Schmid B, Tinevez J-Y, White D J, Hartenstein V, Eliceiri K, Tomancak P and Cardona A 2012 Fiji: an open-source platform for biological-image analysis *Nature Methods* **9** 676

[56] Sternberg S R 1983 Biomedical image processing *Computer* **16** 22-34

[57] Ollion J, Cochennec J, Loll F, Escude C and Boudier T 2013 TANGO: a generic tool for high-throughput 3D image analysis for studying nuclear organization *Bioinformatics* **29** 1840-1

[58] Bolte S and CordeliÈRes F P 2006 A guided tour into subcellular colocalization analysis in light microscopy *Journal of Microscopy* **224** 213-32

[59] Katt M E, Placone A L, Wong A D, Xu Z S and Searson P C 2016 In Vitro Tumor Models: Advantages, Disadvantages, Variables, and Selecting the Right Platform *Front Bioeng Biotechnol* **4** 12

[60] Chignola R and Foroni R I 2005 Estimating the growth kinetics of experimental tumors from as few as two determinations of tumor size: implications for clinical oncology *IEEE Trans Biomed Eng* **52** 808-15

[61] Vinci M, Gowan S, Boxall F, Patterson L, Zimmermann M, Court W, Lomas C, Mendiola M, Hardisson D and Eccles S A 2012 Advances in establishment and analysis of three-dimensional tumor spheroid-based functional assays for target validation and drug evaluation *BMC Biology* **10** 29

[62] Barbier de Reuille P, Routier-Kierzkowska A-L, Kierzkowski D, Bassel G W, Schüpbach T, Tauriello G, Bajpai N, Strauss S, Weber A, Kiss A, Burian A, Hofhuis H, Sapala A, Lipowczan M, Heimlicher M B, Robinson S, Bayer E M, Basler K, Koumoutsakos P, Roeder A H K, Aegerter-Wilmsen T, Nakayama N, Tsiantis M, Hay A, Kwiatkowska D, Xenarios I, Kuhlemeier C and Smith R S 2015 MorphoGraphX: A platform for quantifying morphogenesis in 4D *eLife* **4** e05864

[63] Sanfilippo S, Canis M, Ouchchane L, Botchorishvili R, Artonne C, Janny L and Brugnon F 2011 Viability assessment of fresh and frozen/thawed isolated human follicles:

reliability of two methods (Trypan blue and Calcein AM/ethidium homodimer-1) *J Assist Reprod Genet* **28** 1151-6
[64] Katja H, Shengmao L, Liesbeth T, Sandra Van V, Linxia G and Aleksandr O 2016 Bioink properties before, during and after 3D bioprinting *Biofabrication* **8** 032002
[65] Miller J S and Burdick J A 2016 Editorial: Special Issue on 3D Printing of Biomaterials *ACS Biomaterials Science & Engineering* **2** 1658-61
[66] Jose R R, Rodriguez M J, Dixon T A, Omenetto F and Kaplan D L 2016 Evolution of Bioinks and Additive Manufacturing Technologies for 3D Bioprinting *ACS Biomaterials Science & Engineering* **2** 1662-78
[67] Guvendiren M, Molde J, Soares R M D and Kohn J 2016 Designing Biomaterials for 3D Printing *ACS Biomaterials Science & Engineering*
[68] Lewis J A 2006 Direct Ink Writing of 3D Functional Materials *Advanced Functional Materials* **16** 2193-204
[69] Coussot P 2005 *Rheometry of pastes, suspensions, and granular materials : applications in industry and environment* (Hoboken, N.J.: Wiley)
[70] Mouser V H, Melchels F P, Visser J, Dhert W J, Gawlitta D and Malda J 2016 Yield stress determines bioprintability of hydrogels based on gelatin-methacryloyl and gellan gum for cartilage bioprinting *Biofabrication* **8** 035003
[71] Jabbari E, Sarvestani S K, Daneshian L and Moeinzadeh S 2015 Optimum 3D Matrix Stiffness for Maintenance of Cancer Stem Cells Is Dependent on Tissue Origin of Cancer Cells *PLoS One* **10** e0132377
[72] Liu J, Tan Y, Zhang H, Zhang Y, Xu P, Chen J, Poh Y C, Tang K, Wang N and Huang B 2012 Soft fibrin gels promote selection and growth of tumorigenic cells *Nature Materials* **11** 734-41
[73] Guzman A, Ziperstein M J and Kaufman L J 2014 The effect of fibrillar matrix architecture on tumor cell invasion of physically challenging environments *Biomaterials* **35** 6954-63
[74] Yeh Y C, Ling J Y, Chen W C, Lin H H and Tang M J 2017 Mechanotransduction of matrix stiffness in regulation of focal adhesion size and number: reciprocal regulation of caveolin-1 and beta1 integrin *Scientific Reports* **7** 15008
[75] Paszek M J, Zahir N, Johnson K R, Lakins J N, Rozenberg G I, Gefen A, Reinhart-King C A, Margulies S S, Dembo M, Boettiger D, Hammer D A and Weaver V M 2005 Tensional homeostasis and the malignant phenotype *Cancer Cell* **8** 241-54
[76] Friedrich J, Seidel C, Ebner R and Kunz-Schughart L A 2009 Spheroid-based drug screen: considerations and practical approach *Nat Protoc* **4** 309-24
[77] Tavares S, Vieira A F, Taubenberger A V, Araujo M, Martins N P, Bras-Pereira C, Polonia A, Herbig M, Barreto C, Otto O, Cardoso J, Pereira-Leal J B, Guck J, Paredes J and Janody F 2017 Actin stress fiber organization promotes cell stiffening and proliferation of pre-invasive breast cancer cells *Nature communications* **8** 15237
[78] Padilla-Rodriguez M, Parker S S, Adams D G, Westerling T, Puleo J I, Watson A W, Hill S M, Noon M, Gaudin R, Aaron J, Tong D, Roe D J, Knudsen B and Mouneimne G 2018 The actin cytoskeletal architecture of estrogen receptor positive breast cancer cells suppresses invasion *Nature communications* **9** 2980
[79] Bao M, Xie J, Piruska A and Huck W T S 2017 3D microniches reveal the importance of cell size and shape *Nature communications* **8** 1962